ADVANCED ENERGY MATERIALS
www.advenergymat.de

Smart Dope: A Self-Driving Fluidic Lab for Accelerated Development of Doped Perovskite Quantum Dots

*Fazel Bateni, Sina Sadeghi, Negin Orouji, Jeffrey A. Bennett, Venkat S. Punati, Christine Stark, Junyu Wang, Michael C. Rosko, Ou Chen, Felix N. Castellano, Kristofer G. Reyes, and Milad Abolhasani**

Metal cation-doped lead halide perovskite (LHP) quantum dots (QDs) with photoluminescence quantum yields (PLQYs) higher than unity, due to quantum cutting phenomena, are an important building block of the next-generation renewable energy technologies. However, synthetic route exploration and development of the highest-performing QDs for device applications remain challenging. In this work, Smart Dope is presented, which is a self-driving fluidic lab (SDFL), for the accelerated synthesis space exploration and autonomous optimization of LHP QDs. Specifically, the multi-cation doping of $CsPbCl_3$ QDs using a one-pot high-temperature synthesis chemistry is reported. Smart Dope continuously synthesizes multi-cation-doped $CsPbCl_3$ QDs using a high-pressure gas-liquid segmented flow format to enable continuous experimentation with minimal experimental noise at reaction temperatures up to 255°C. Smart Dope offers multiple functionalities, including accelerated mechanistic studies through digital twin QD synthesis modeling, closed-loop autonomous optimization for accelerated QD synthetic route discovery, and on-demand continuous manufacturing of high-performing QDs. Through these developments, Smart Dope autonomously identifies the optimal synthetic route of Mn-Yb co-doped $CsPbCl_3$ QDs with a PLQY of 158%, which is the highest reported value for this class of QDs to date. Smart Dope illustrates the power of SDFLs in accelerating the discovery and development of emerging advanced energy materials.

1. Introduction

Colloidal inorganic lead halide perovskite (LHP) quantum dots (QDs) represent a class of highly advanced functional materials renowned for their facile solution processing and multifaceted applications in a broad spectrum of photonic and energy devices.[1–4] These ionic QDs exhibit exceptional optoelectronic properties, prominently characterized by their high photoluminescence quantum yield (PLQY), narrow emission linewidth, and the ability to tune their emission color through size and compositional modifications.[5,6] Consequently, they serve as versatile building blocks for an extensive array of optoelectronic applications, including light emitting diodes,[7,8] lasers,[9] photodetectors,[10] and luminescent solar concentrators (LSCs).[11–13]

Impurity metal cation doping has emerged as a promising strategy for enhancing and tailoring the application-specific properties of LHP QDs with high precision and versatility.[14,15] Transition metal and lanthanide ions, such as

F. Bateni, S. Sadeghi, N. Orouji, J. A. Bennett, V. S. Punati, C. Stark, M. Abolhasani
Department of Chemical and Biomolecular Engineering
North Carolina State University
Raleigh, NC 27695-7905, USA
E-mail: abolhasani@ncsu.edu

J. Wang, O. Chen
Department of Chemistry
Brown University
Providence, RI 02912, USA

M. C. Rosko, F. N. Castellano
Department of Chemistry
North Carolina State University
Raleigh, NC 27695-8204, USA

K. G. Reyes
Department of Materials Design and Innovation
University at Buffalo
Buffalo, NY 14260, USA

The ORCID identification number(s) for the author(s) of this article can be found under https://doi.org/10.1002/aenm.202302303

DOI: 10.1002/aenm.202302303

manganese (Mn^{2+}) and ytterbium (Yb^{3+}), when incorporated into LHP QDs as metal cation dopants, not only introduce additional emission windows induced by the internal Mn *d-d* and Yb *f-f* states within the visible and near-infrared (NIR) regions, but also introduce novel magnetic and down-conversion properties to the host LHP QDs.[16–24] Specifically, cesium lead chloride ($CsPbCl_3$) QDs which possess the highest bandgap among other metal halide perovskite candidates, provide a more efficient energy transfer to the internal *d-d* and *f-f* states, thereby making it an ideal host for metal cation doping. This unique and tunable integration of impurity metal cations significantly enhances light harvesting and down-conversion capabilities of LHP QDs, leading to their improved performance in energy devices, particularly downconverters, and LSCs.[11,17]

The incorporation of multiple impurity metal cation dopants into the expansive synthesis reaction space of LHP QDs introduces a significantly larger explorative experimental space arising from the diverse range of metal cations, dopant concentrations, and doping ratios that can be employed in addition to the synthetic reaction space of pristine LHP QDs.[25–28] The multifaceted role of synthesis parameters on the optical properties of the resulting QDs makes comprehensive exploration of the multicomponent QDs even more challenging. Consequently, the exploration, development, synthetic route discovery, and optimization of multi-cation-doped LHP QDs with conventional batch-based trial-and-error methods are time-consuming and labor-intensive and lead to substantial materials consumption (cost) and waste generation.[29–31] Clearly, conventional one-at-a-time manual experimentation methods are inadequate to reach the required development pace of LHP QDs. Thus, there is a significant need for an alternative materials development platform.

The recent emergence of machine learning (ML)-assisted closed-loop experimentation approaches, known as self-driving labs (SDLs), offers a promising solution to expedite the pace of materials discovery, development, and optimization.[32–38] These autonomous experimentation platforms leverage process automation and advanced ML algorithms to automate the experimental workflow iteration of hypothesis formulation, experimental planning and selection, execution of the selected experiments, and analysis of the experimental results. SDLs pave the way for accelerated materials research and development by facilitating high-throughput and data-driven exploration of the chemical space.[39–42] Over the past three years, proof-of-concept SDLs utilizing batch reactors have been demonstrated for rapid exploration and synthesis of advanced functional materials, including metallic and semiconductor nanoparticles and thin-film materials.[43–47]

The majority of existing SDLs for materials development have relied mainly on batch-based experimentation techniques. However, batch reactors inherently suffer from several limitations, including the discontinued nature of experimentation, irreproducible heat and mass transfer rates, and limited accessibility for in situ characterization techniques, resulting in materials-, cost-, and time-intensive procedures within an SDL.[25,27,48] These issues are even more manifested in the synthesis of multi-cation-doped LHP QDs due to their fast nanocrystal formation kinetics and the inefficient mixing environment in conventional batch reactors. A key requirement of SDLs to accelerate the pace of materials discovery, development, and optimization is access to high-quality experimental data with minimum experimental noise.[33,36] These high-fidelity experimental data serve as the foundational pillars for data science tools of SDLs employed for automated modeling and subsequent experiment-selection tasks within the autonomous experimentation approach. However, the time-consuming nature of manual or even automated sampling from batch reactors presents a significant bottleneck in providing the necessary large volume of high-quality experimental data to ML algorithms embedded in SDLs, impeding their ability to navigate accurately and efficiently within the vast chemical space of colloidal QDs.[5,49]

Alternatively, microscale flow chemistry strategies offer a more favorable technological solution for accelerated materials development with SDLs.[25,32,34,38] Additionally, flow chemistry platforms enable facile integration of multimodal in situ and/or online material characterization probes, efficient process automation, and reliable and accurate reaction control.[26,31,33] These unique advantages, directly related to the quality and quantity of experimental data required for the ML algorithms of SDLs, make flow reactors an ideal tool for accelerated materials development. Therefore, navigating the autonomous experimentation technologies toward self-driving fluidic labs (SDFLs) represents an ideal path for the fast-tracked discovery, development, and optimization of multi-cation doped LHP QDs.[35,36]

This study presents Smart Dope, which is an SDFL for the accelerated development of multi-cation-doped LHP QDs. Specifically, we focus on synthesizing and optimizing Mn-Yb co-doped LHP QDs using a one-pot heat-up synthesis technique. Smart Dope leverages a modular flow chemistry platform as its core hardware and an ensemble neural network (ENN) as its ML tool for input (synthesis parameters)-output (PLQY) mapping of multi-cation-doped LHP QDs. Additionally, Smart Dope is equipped with Bayesian optimization for autonomous synthetic route optimization of colloidal QDs. Smart Dope rapidly investigates the complex synthesis space of Mn-Yb co-doped $CsPbCl_3$ QDs and autonomously unveils the optimal synthetic route resulting in the highest PLQY reported to date (158%). First, Smart Dope automatically screens the experimental synthesis space of QDs via Latin hypercube sampling (LHS). The LHS provides in-house generated experimental data for building an ML model (digital twin) of the multi-cation doping chemistry that is subsequently used for both mechanistic and fundamental studies of the multi-cation-doped LHP QDs. Next, Smart Dope utilizes its automatically generated multi-cation doping chemistry knowledge to autonomously optimize the total PLQY of multi-cation-doped LHP QDs iteratively via Bayesian optimization. Smart Dope demonstrates a rapid and intelligent exploration of a vast experimentally accessible parameter space of multi-cation-doped LHP QDs, exceeding over 1.9×10^{13} potential synthetic conditions (Figure S2, Supporting Information). The autonomous search through the multivariate experimental space of advanced functional materials using the developed SDFL not only saves significant time, precursor resources, and labor but also yields high-performance multi-cation-doped LHP QDs that serve as exceptional building blocks for the fabrication of printed photonic devices employed in light-harvesting applications.

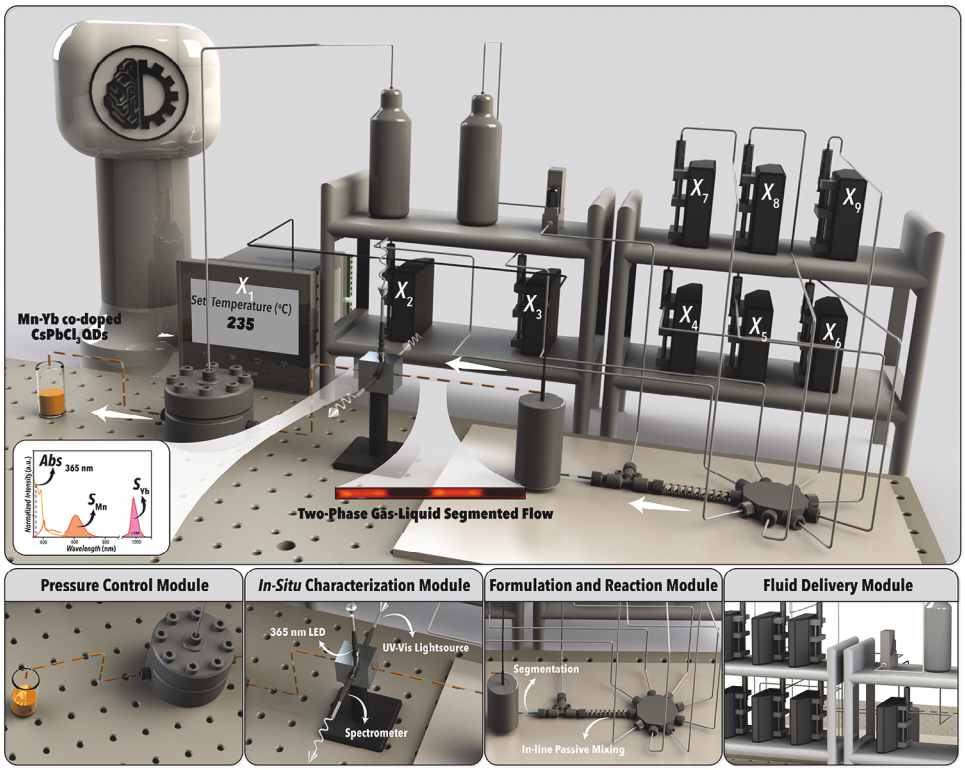

Figure 1. Schematic illustration of Smart Dope's modular hardware, including the fluid delivery, X_2-X_9, formulation and reaction, in situ characterization, temperature controller, X_1, and pressure control modules.

2. Results and Discussion

2.1. Smart Dope Hardware

Smart Dope's hardware, illustrated in **Figure 1**, is built on a flow chemistry platform comprising four key modules: fluid delivery, formulation and reaction, in situ characterization, and pressure control. In the fluid delivery module, eight syringe pumps equipped with gas-tight stainless steel syringes were utilized to guide the liquid precursors at specific volumetric flow rates through a 9-way fluidic manifold. A two-phase gas-liquid segmented flow was generated within the formulation and reaction module by combining the mixed QD precursors stream as the reactive phase and argon (Ar) gas as the inert carrier phase at a T-junction. Additional details of the experimental setup and precursor concentrations can be found in the Experimental Section. The formed gas-liquid segmented flow was directed into a stainless steel flow reactor, maintained at temperatures ranging from 160 °C to 255 °C. The main reaction followed a one-pot heat-up synthetic approach, with the residence time (t_R) in the flow reactor varying between 15 s to 42 s, depending on the total liquid and gas flow rates. Smart Dope could explore 250 different experimental conditions with a single batch of the QD precursors. The automated synthesis of multi-cation-doped LHP QDs was achieved by controlling nine independent input parameters, including reaction temperature and volumetric flow rates of the eight liquid precursors (cesium acetate: [Cs], lead acetate: [Pb], chlorotrimethylsilane: [Cl], manganese acetate: [Mn], ytterbium acetate: [Yb], oleic acid: [OA], oleylamine: [OAm], 1-octadecene: [ODE]). To ensure consistent slug formation at different reaction temperatures and residence (synthesis) times in the flow reactor, the volumetric flow rate of the inert carrier gas was automatically adjusted based on the total liquid volumetric flow rates and a constant gas-to-liquid volumetric ratio. Following the in-flow synthesis at high temperatures, the reactive liquid slugs containing Mn-Yb co-doped $CsPbCl_3$ QDs were rapidly cooled to room temperature before entering the in situ characterization module, where their UV-vis-NIR absorption and photoluminescence (PL) spectra were recorded automatically. Finally, the reactor's outlet was connected to a back-pressure regulator (BPR) operating at 95 psig using nitrogen (N_2) gas to minimize the expansion of the carrier gas phase at high reaction temperatures and ensure uniform liquid slug formation throughout the in-flow synthesis and online characterization processes. Thermal quenching offered by the enhanced cooling rate of the microscale flow reactor was utilized for rapid termination of the in-flow synthesized QDs.[28] Figure S1 (Supporting Information) shows the assembly of Smart Dope's modular flow chemistry hardware for autonomous high-temperature synthesis of Mn-Yb co-doped LHP QDs.

Next, we will discuss the robustness and reproducibility of Smart Dope's hardware, which are foundational to achieving closed-loop autonomous experimentation. We will then present the integration of the Smart Dope's hardware with Bayesian optimization, leading to the creation of an SDFL capable of autonomous synthetic route discovery, optimization, and continuous manufacturing of multi-cation-doped LHP QDs.

Impurity metal cation doping of LHP QDs with lanthanide ions results in the emergence of an additional emission peak in the NIR region of the PL spectrum.[17,19] This new emission peak arises from incorporating *f-f* states within the bandgap (BG) of LHP QDs, particularly when lanthanide dopants such as Yb^{3+} ions are utilized. Developing a reliable in situ spectral characterization method capable of accurately capturing PL spectra of lanthanide-doped LHP QDs becomes imperative for autonomous experimentation. Specifically, it is crucial to develop an in situ QD characterization technique that closely matches the accuracy of more powerful benchtop spectrometers. In this regard, we have devised a spectral benchmarking approach to align and correct the in situ measured PL spectra of the multi-cation-doped LHP QDs versus offline measurements. Detailed information regarding the in situ spectral validation can be found in the Supporting Information (Figure S4, Supporting Information). The primary objective of this study is to identify the most optimal Mn-Yb co-doped LHP QDs with enhanced optical properties, particularly focusing on achieving the highest PLQY. To achieve this objective, leveraging the benchmarked in situ UV-vis-NIR absorption and PL spectroscopy module, we developed an in situ PLQY measurement strategy and validated it against offline absolute PLQY measurements for the same multi-cation-doped LHP QDs. This in situ relative PLQY measurement technique enabled real-time calculation of individual PLQY values corresponding to the BG, Mn, and Yb emissions. Further details regarding the relative PLQY calculations can be found in the Supporting Information (Figure S5, Supporting Information).

2.2. Hardware Automation

Developing robust process automation is crucial to building a fully closed-loop autonomous experimentation framework as the foundation of Smart Dope. This process automation workflow should encompass experimental execution, data acquisition, and data analysis. The process automation workflow of Smart Dope was developed to maintain 24/7 control over the operation of the modular flow chemistry setup. The custom-developed process automation of Smart Dope (LabVIEW, see Figure S6, Supporting Information) was coupled with a Python script for automatic parsing of experimental conditions, process operation, data recording, and data analysis to obtain real-time spectral information of the in-flow synthesized Mn-Yb co-doped $CsPbCl_3$ QDs. The process automation of Smart Dope included starting the flow of QD precursors into the reactor once the system reached a steady-state temperature. Additionally, Smart Dope was equipped with the automatic acquisition of UV-vis-NIR absorption and PL spectra after the equilibrium waiting time (t_E), which guarantees data recording occurs when the flow reactor's Mn-Yb co-doped LHP QDs synthesis reaction has reached steady-state. Furthermore, Smart Dope's operation workflow incorporated an automated intermittent flow reactor washing protocol to ensure consistent and reproducible reactor performance, enabling uniform and high-quality continuous manufacturing of multi-cation-doped LHP QDs over long-term operation while preventing nanocrystal precipitation and reactor fouling.

2.3. Ex Situ Characterization of the In-Flow Synthesized QDs

Next, Smart Dope was utilized to synthesize two samples of pristine $CsPbCl_3$ QDs and Mn-Yb co-doped $CsPbCl_3$ QDs for ex situ structural characterizations to verify the successful one-pot colloidal synthesis of multi-cation-doped LHP QDs (Figure S6, Supporting Information). The in-flow synthesized QDs were then utilized for a detailed analysis of luminescence properties and colloidal stability of undoped and Mn-Yb co-doped $CsPbCl_3$ QDs (see Figure S6, Supporting Information). The transmission electron microscopy (TEM) images, along with their corresponding histograms depicted in Figure S6A,B (Supporting Information), demonstrate a uniform cubic morphology for both the pristine and Mn-Yb co-doped $CsPbCl_3$ QDs with an average edge length of 9.79±1.53 nm and 8.53±1.22 nm, respectively. Table S1 and S2 (Supporting Information) provide a summary of the energy-dispersive X-ray spectroscopy (EDS) analysis conducted on the surfaces of the doped and undoped samples, confirming the successful incorporation of Mn^{2+} and Yb^{3+} ions into the crystalline structure while maintaining an atomic ratio similar to that of pristine $CsPbCl_3$ QDs. Figure S6C (Supporting Information) presents the X-ray diffraction (XRD) patterns of undoped $CsPbCl_3$ QDs and Mn-Yb co-doped $CsPbCl_3$ QDs, providing evidence of a pure crystalline cubic phase that remains unaffected during the metal cation doping process.[11,50] Notably, the XRD peaks of the multi-cation-doped QDs exhibit a slight forward shift, attributed to the impact of cation doping with Mn^{2+} and Yb^{3+} ions, which possess smaller ionic radii compared to Pb^{2+} ions. As a result of substituting Pb^{2+} ions with impurity metal cation dopants, there is a reduction in the crystalline size, consistent with the average nanocrystal size observed in the TEM images.[11,50] These peak shifts and size reductions signify a homogeneous metal cation doping mechanism, wherein the dopants diffuse inward into the crystalline structure rather than residing solely on the surface of the host nanocrystals, which would indicate heterogeneous doping.[50] Moreover, the presence of six hyperfine splitting profiles (A = 88 G) in the electron paramagnetic resonance (EPR) spectrum of the multi-cation-doped LHP QD sample with respect to the absence of any EPR peaks for the pristine QDs (Figure S6D, Supporting Information) demonstrates the successful incorporation of Mn^{2+} ions into the cubic structure of $CsPbCl_3$ QDs following a homogenous doping mechanism achieved via Smart Dope.[50] In order to further verify the successful multi-cation doping of LHP QDs, the in-flow synthesized QDs were characterized via X-ray photoelectron spectroscopy (XPS). XPS spectra of the co-doped $CsPbCl_3$ QDs presented in Figure S6E–I (Supporting Information) provide evidence of the successful incorporation of Mn^{2+} and Yb^{3+} ions into the host $CsPbCl_3$ QDs following the high-temperature in-flow metal cation doping process. The ex situ structural characterizations of the in-flow synthesized QDs by Smart Dope demonstrates the success of the developed flow chemistry strategy in facilitating the incorporation of impurity transition and lanthanide metal cations into the crystalline structure of the host LHP QDs.

2.4. Hardware Characterization and Reproducibility

In the next step, we conducted a comprehensive study of the performance and reliability of Smart Dope's hardware for the

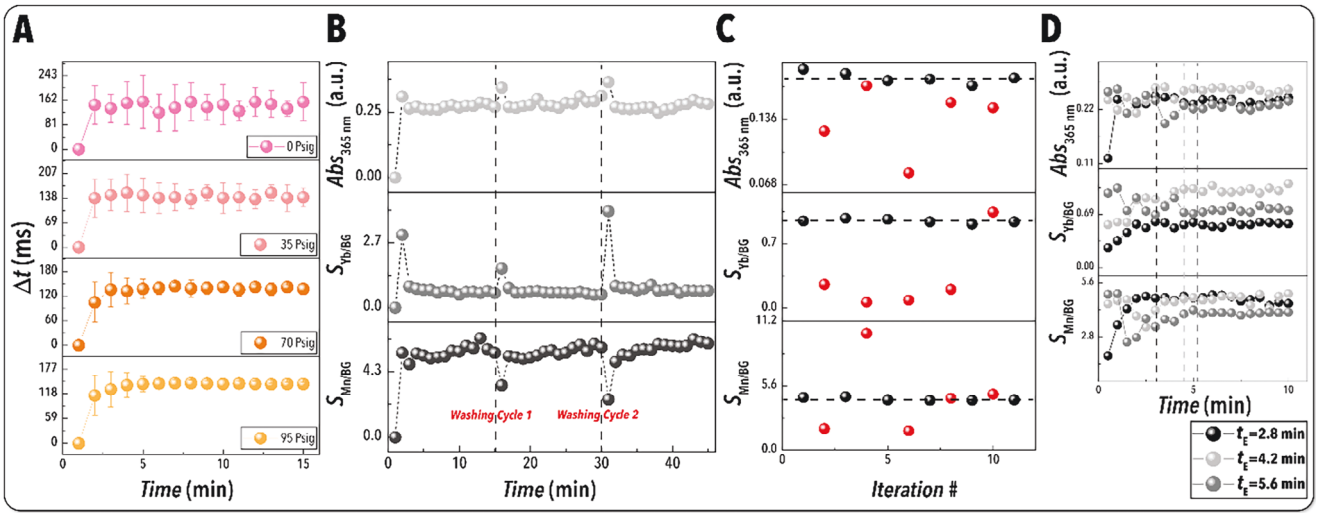

Figure 2. Characterization of Smart Dope's hardware regarding flow formation stability, precision, and reproducibility: A) Effect of reaction pressure on the temporal evolution of reactive phase travel time. B) Temporal evolution of Abs_{365nm}, $S_{Mn/BG}$, and $S_{Yb/BG}$ for a constant QD synthesis condition over 60 min. C) Assessment of Smart Dope's QD synthesis reproducibility for a constant synthesis condition (black dots) following the application of 5 randomly selected (red dots) synthesis conditions. D) Examination of the impact of dynamic residence time to determine the multiple of residence times required to wait before reaching steady-state operation applicable to all autonomous conditions.

automated synthesis of advanced energy materials. Specifically, we focused on three key aspects: i) ensuring proper mixing and uniform flow segmentation, ii) establishing reliable continuous operation, and iii) achieving reproducible in-flow QD synthesis. These investigations provide substantial evidence for the viability of long-term continuous operation of Smart Dope's hardware before conducting autonomous experimentation.

As part of the flow system characterization, the stability and uniformity of the gas-liquid segmented flow were investigated. The temporal PL intensities were monitored continuously at a specific wavelength (400 nm) for 15 min to visually distinguish the reactive phase from the inert gas phase and assess the averaged travel time for 1 min. This segmented flow characterization technique, illustrated in Figure S7 (Supporting Information), enabled the identification of the passage of inert gas and reactive phase slugs. Next, we studied the effect of varying the reaction pressure via a back-pressure regulator attached to the segmented flow reactor outlet on the uniformity of the reactive phase liquid slugs (**Figure 2**A). It is evident from the results shown in Figure 2A that only operating at reactor pressures higher than 70 psig ensures a uniform flow segmentation. Considering the importance of uniform mixing rates in the segmented flow reactor for achieving consistent quality of Mn-Yb co-doped LHP QDs, the back-pressure regulator was set at 95 psig to ensure uniform average flow velocity for both gas and liquid segments (i.e., constant residence time) once the system reaches steady-state operation. It is worth noting that the steady-state time for the studies shown in Figure 2A was measured when only the precursor lines were filled, and the reactor's outlet contained no slugs from previous in-flow QD synthesis experiments.

The reliability of Smart Dope's hardware for the continuous synthesis of Mn-Yb co-doped LHP QDs was assessed using three optical features obtained in situ (Figure 1): the absorbance value at 365 nm (Abs_{365nm}, reaction yield proxy), the area ratio of the Mn to BG emission peak ($S_{Mn/BG}$, Mn emission proxy), and the area ratio of the Yb to the BG emission peak ($S_{Yb/BG}$, Yb emission proxy). Normalizing the peak emissions areas of the Mn and Yb emission peaks with respect to the BG emission peak enabled relative analysis of PLQY values of the co-doped LHP QDs at different synthesis conditions (required for autonomous optimization), independent of the absolute PL emission area values. Figure 2B illustrates Smart Dope's response for all three in situ obtained optical features (Abs_{365nm}, $S_{Mn/BG}$, $S_{Yb/BG}$) of Mn-Yb co-doped $CsPbCl_3$ QDs, with standard deviations 3.6%, 4.9%, 4.8%, respectively after implementing a washing cycle every 15 min and allowing sufficient transient time (≈5 min) to reach the steady-state operation. The intermittent automated washing protocol, performed every 15 min on the stream of Smart Dope, effectively prevents QDs' precipitation and reactor fouling, ensuring the flow system's long-term operational stability for Smart Dope's autonomous experimentation mode.

Next, to assess the reproducibility of Smart Dope's performance regarding its automated process operation and reproducibility of the in situ spectral response for a given QD synthesis condition, an experimental perturbation study was conducted with five randomly specified QD synthesis conditions sequentially performed between a constant reference synthesis condition. Figure 2C demonstrates the capability of Smart Dope's flow chemistry hardware to reproduce consistent responses for all three output optical features, with standard deviations 3.3%, 3.2%, and 2.5%, respectively. This result highlights the robustness and reliability of Smart Dope's hardware in achieving reproducible results, which is an important feature for minimizing the experimental noise of SDLs.

In order to determine the appropriate equilibrium time for initiating in situ characterization of the in-flow synthesized QDs, it is essential to establish the multiple residence times needed for a given QD synthesis condition in Smart Dope to reach steady-state operation. Thus, three QD synthesis conditions were tested in a sequence with nominal residence times of 0.93 min, 1.4 min, and

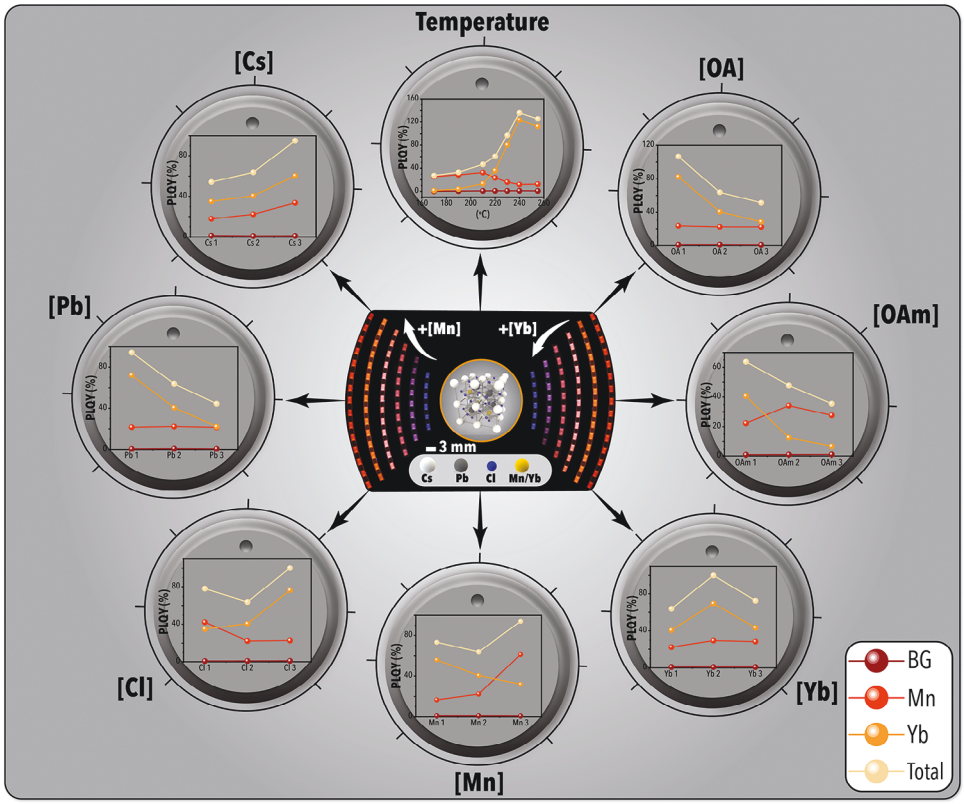

Figure 3. Automated in-flow exploration of the vast reaction space of multi-cation-doped LHP QDs. The presented PLQY results show the complexity of the high-dimensional Mn-Yb co-doped $CsPbCl_3$ QD synthesis which underscores the necessity for accelerated optimization through advanced autonomous experimentation by Smart Dope.

1.86 min. The optical features of the three tested QD synthesis conditions, presented in Figure 2D, illustrate that the flow chemistry platform consistently reaches steady-state operation before 3× the nominal residence time of a given QD synthesis condition. Finally, the long-term stability of the QD precursors was tested over five days for a single synthesis condition. Figure S8A,B (Supporting Information) exhibits consistent spectral responses for the same batch of QD precursors and the same QD synthesis condition over five days, indicating both the stability of the QD precursors and the reliability of Smart Dope's hardware for its autonomous operation over multiple days, see Supporting Information (Figure S9, Supporting Information).

2.5. Automated In-Flow Screening of Multi-Cation-Doped LHP QDs

To glean preliminary insights into the synthesis chemical space of Mn-Yb co-doped LHP QDs, a partial grid search study was conducted using the automated operation mode of Smart Dope. This parameter space exploration study involved only varying an input parameter of interest while keeping the remaining input parameters constant and measuring the corresponding PLQYs. The results of this automated parameter space exploration study are summarized in **Figure 3**, which illustrates the impact of each input parameter on the PLQYs as they transition from lower to higher values. The recorded UV-vis-NIR PL and absorption spectra for each partial grid study condition can be found in Figures S9 and S10 (Supporting Information) respectively. Moreover, a summary of the measured PLQYs obtained from the in-flow screening studies is provided in Table S4 (Supporting Information). These preliminary findings offer valuable insights into the metal cation doping mechanism of LHP QDs at high temperatures and facilitate the QD synthesis parameter boundaries adjustment within their respective dimensionless equations. Defining the boundaries of the experimental space facilitates a more efficient and focused autonomous navigation process, reducing the overall experimentation time and minimizing material consumption for subsequent autonomous experimentation campaigns. For instance, increasing the concentration of Cs precursor led to an enhancement in the total PLQY, as it facilitated the formation of more QDs which can be observed from the rise of Abs_{365nm} value (Figure S10A, Supporting Information). Increasing the concentration of Pb precursor also increases the number of formed QDs (Figure S10B, Supporting Information). Still, it limited the diffusion of Yb^{3+} ions within the QDs due to the increased population of free Pb^{2+} ions in the reaction mixture. The concentration of Cl precursor influenced the diffusion of Yb^{3+} ions, suggesting the formation of complexes between Yb^{3+} and Cl^- ions for metal cation insertion into the QD lattice. However, excessive amounts of Cl^- ions and a higher population of free Yb^{3+} ions led to the removal of more Pb^{2+} ions, disrupting the perovskite crystal structure and decreasing the population of

QDs (Figure S10C, Supporting Information). Increasing the concentration of Mn precursor resulted in higher Mn doping levels. Still, it limited the incorporation of Yb^{3+} ions. Subsequently, it restricted the accessible total PLQY, which agrees with the results of Chen et al. where it was demonstrated that high Mn doping levels can quench the Yb-induced emissions.[11] Moreover, increasing the concentration of Yb precursor initially increased the total PLQY, but excessive Yb^{3+} ions acted as a diffusion barrier for further incorporation of metal cation dopants and negatively affected the crystalline integrity of the QDs (Figure S10E, Supporting Information).

Regarding the impact of ligands, increasing the OAm precursor concentration initially increased the Mn doping level, as Mn^{2+} ions were found to form complexes with Oleylamonium ions for exchange with Pb^{2+} ions within the host QDs.[14,51,52] However, an excess of oleylammonium ions could deteriorate the crystalline integrity of the host QDs and limit the incorporation of Yb^{3+} ions.[14,51,52] On the other hand, the concentration of OA precursor had a minor impact on forming more QD hosts. However, by likely bringing freely available Cs^{+} ions into the crystalline structure, increasing the OA precursor concentration can improve the Mn doping level and thereby limit the incorporation of Yb^{3+} ions as a secondary metal cation dopant.

The impact of reaction temperature was also studied, revealing that the maximum Mn doping level was obtained between 190 °C to 210 °C. In comparison, the Yb doping level was limited between 170 °C to 210 °C and exponentially increased between 210 °C to 240 °C. Further increase of the reaction temperature beyond 240 °C diminished the formation of multi-cation-doped LHP QDs and resulted in lower total PLQYs than QDs synthesized at lower temperatures. Additionally, the impact of reaction (residence) time on the PLQY of multi-cation-doped LHP QDs was investigated by varying the reactor's length (volume) at a constant total volumetric flow rate (i.e., similar mixing rate). It was found that the developed one-pot heat-up synthesis approach of multi-metal cation-doped LHP QDs required a reaction time of 17 s to 35 s to achieve the highest PLQY and reaction yield. Prolonging the reaction time beyond 35 s at high reaction temperatures led to reduced metal cation doping levels due to the decomposition of the formed host QDs. Therefore, it is necessary to quench the reaction after 35 s to maintain optimal synthesis conditions. Overall, the automated QD parameter space screening provided valuable knowledge for narrowing down the reaction temperature range for lanthanide doping of LHP QDs. The highest obtained PLQY throughout the automated partial grid search was 136% (also shown in Table S4, Supporting Information), with minimal contribution of the BG PLQY to the total PLQY. These findings motivate further optimization of Mn and Yb doping to maximize the total PLQY of Mn-Yb co-doped $CsPbCl_3$ QDs via the autonomous operation mode of Smart Dope.

2.6. Autonomous Multi-Cation-Doping of LHP QDs

The high-dimensionality of the experimental space associated with Mn-Yb co-doped LHP QDs poses significant challenges in the search for the optimal QD formulation with the highest PLQY. The advent of SDFLs and the implementation of closed-loop autonomous experimentation offer an informed and efficient means of navigating this vast and multivariate parameter space with minimal experimental iterations. Therefore, in the next step, we designed a global learning stage, conducting 150 automated QD synthesis experiments at reaction conditions selected by LHS to provide unbiased experimental data from the accessible QD synthesis experimental space. The LHS experimental data was then utilized for building a digital twin of the one-pot multi-cation QD doping reaction and an accurate surrogate model for subsequent closed-loop optimization campaigns. To address the chemical space's complexity, we focused on optimizing three key optical properties of the in-flow synthesized QDs: Abs_{365nm}, S_{Mn}, and S_{Yb}. These three process outputs were then transformed into total PLQY to maximize its value. Mapping these in situ measured QD optical features to the synthesis input parameters (X_i, i = 1-9) was achieved through an ML approach, employing an ENN with fine-tuned hyperparameters (see (Section S1.2, Supporting Information)).

The ENN model trained on the LHS experimental data generated in-house by Smart Dope served to: i) create a belief model, representing the digital twin of Smart Dope's physical hardware for fundamental mechanistic studies of the multi-cation LHP QD synthesis and ii) guide the subsequent experimental selections for closed-loop autonomous optimization campaigns. The trained digital twin not only provided precise predictions (R^2>0.87) for the QD optical features of interest (i.e., Smart Dope's outputs) but also offered valuable mechanistic insights into the metal cation doping reaction. **Figure 4**A–F presents the performance (accuracy) of the trained digital twin for both the training and test data sets. Table S5 (Supporting Information) shows all the experimental conditions with the measured PLQY values obtained via the automated LHS experiments.

2.7. Discussion

The next step involved utilizing the digital twin knowledge to further our understanding of the fundamental mechanistic aspects of Mn-Yb co-doped LHP QD synthesis chemistry. The trained ENN digital twin generated Shapley additive explanation plots for each QD optical feature (process output), ranking the importance of QD synthesis input parameters from highest to lowest (**Figure 5**A) for the precursor chemistry employed in this study. It should be noted that the results of Shapley additive explanation plots of the reaction parameters should be considered along with the nanocrystal synthesis science of QDs to facilitate a better understanding of the role of synthesis input parameters on the resulting optical properties and performance of the product (multi cation-doped LHP QDs). Therefore, although all synthesis input parameters are found to affect the output properties of the in-flow synthesized QDs (Figures 3 and 5), we limited our analysis only to the most significant model features with the largest SHAP value span. The Shapley analysis in Figure 5A suggests that Pb and Cl precursors' concentration represents the most important QD synthesis input parameters affecting $Abs_{365\ nm}$ of Mn-Yb co-doped $CsPbCl_3$ QDs. The Shapley analysis results, generated from the ENN digital twin model of the multi-cation-doped LHP QDs, are well-aligned with the formation mechanism of LHP QDs, where Pb and Cl are the key elements of the host QD structure and play a crucial role in determining the reaction yield of the one-pot QD

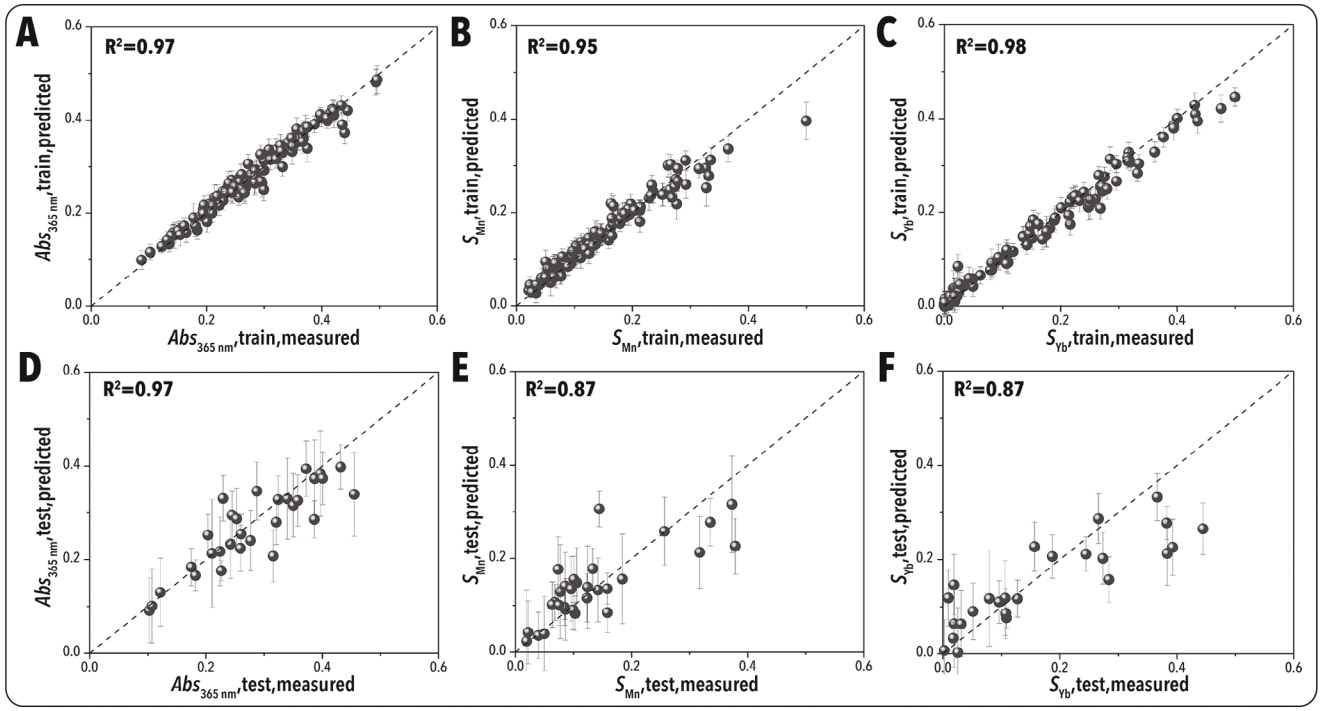

Figure 4. Performance of the digital twin trained using the in-house generated LHS experimental data. Parity plot for measured and predicted output values of the training data sets for A) $Abs_{365\ nm}$, B) S_{Mn}, and C) S_{Yb}. Parity plot for measured and predicted output values of the test data sets for E) $Abs_{365\ nm}$, F) S_{Mn}, and G) S_{Yb}.

synthesis route. This finding is also consistent with the outcomes of our partial grid search experiments (Figure S10A–C, Supporting Information). Analyzing the distribution of SHAP values in Figure 5A, it is evident that increasing the concentrations of Pb precursor leads to greater QDs formation (higher $Abs_{365\ nm}$) by potentially enhancing the nucleation rate of the host LHP QDs. On the other hand, excessive Cl^- ions harm the structural integrity of the LHP QDs. Examining the importance of QD synthesis input parameters for controlling Mn doping (S_{Mn}) using Shapley analysis (Figure 5B), reaction temperature and Mn and Pb precursor concentrations were the most important input parameters. Here, increasing reaction temperature leads to a decrease in Mn doping level. At the same time, higher concentrations of Mn^{2+} and Pb^{2+} ions facilitate successful metal cation exchange between Mn^{2+} and Pb^{2+} ions, resulting in higher Mn doping levels (higher S_{Mn}). Shapley analysis results of S_{Yb}, shown in Figure 5C, suggest that reaction temperature and Pb precursor concentration are the key synthesis input parameters affecting the Yb emission peak of Mn-Yb co-doped $CsPbCl_3$ QDs. Furthermore, the results of Figure 5C reveals that higher Yb doping levels (higher S_{Yb}) require higher reaction temperatures and higher concentration of Pb^{2+} ions. Although increasing Cl^- ion concentration initially enhances Yb doping, excessive amounts deteriorate the QD structure, resulting in lower Yb doping levels. It is worth noting that the concentration of the Yb precursor is not ranked as highly important in controlling S_{Yb} (Figure 5C), which suggests the initial concentration used by Smart Dope was high.

The digital twin studies provide valuable insights into the rational design of QD precursors for enhanced performance. Additionally, the digital twin facilitates visualization of the complex and high-dimensional multi-cation-doped LHP QDs. Figure 5D–F presents a visualization of one-pot multi-cation doping reaction using the digital twin built by the in-house generated experimental data by Smart Dope. Specifically, the impact of the top two ranked synthesis input parameters (based on Shapley analysis) was examined at three levels (low, medium, and high) of the third most important input parameter for each QD optical feature. Figure 5D illustrates that increasing the concentrations of Pb and Cl precursors improves and deteriorates the reaction yield of the host QDs, respectively, in agreement with our previous results and discussions. In addition, increasing the concentration of Cs precursor enhances the reaction yield. Figure 5E demonstrates that the maximum Mn doping level can be achieved between 180 °C to 190 °C, particularly at high levels of Pb precursor concentration. Similarly, high reaction temperatures combined with a medium value of Pb precursor concentration result in the highest Yb doping level of Mn-Yb co-doped $CsPbCl_3$ QDs. Interestingly, an increase in Cl precursor concentration can also result in higher Yb doping, possibly due to the formation of coordination complexes between Yb^{3+} and Cl^- ions, facilitating successful metal cation exchange between Yb^{3+} and Pb^{2+} ions.

Following the digital twin studies of multi-cation-doped LHP QDs, the trained ENN model was utilized as a surrogate model for autonomous PLQY optimization by Smart Dope. The goal of this autonomous QD synthesis campaign was to utilize the in-house generated prior knowledge from the LHS experiments to rapidly identify the most optimal synthetic route of Mn-Yb co-doped $CsPbCl_3$ QDs with the highest PLQY while minimizing the number of experimental iterations (experimental cost).

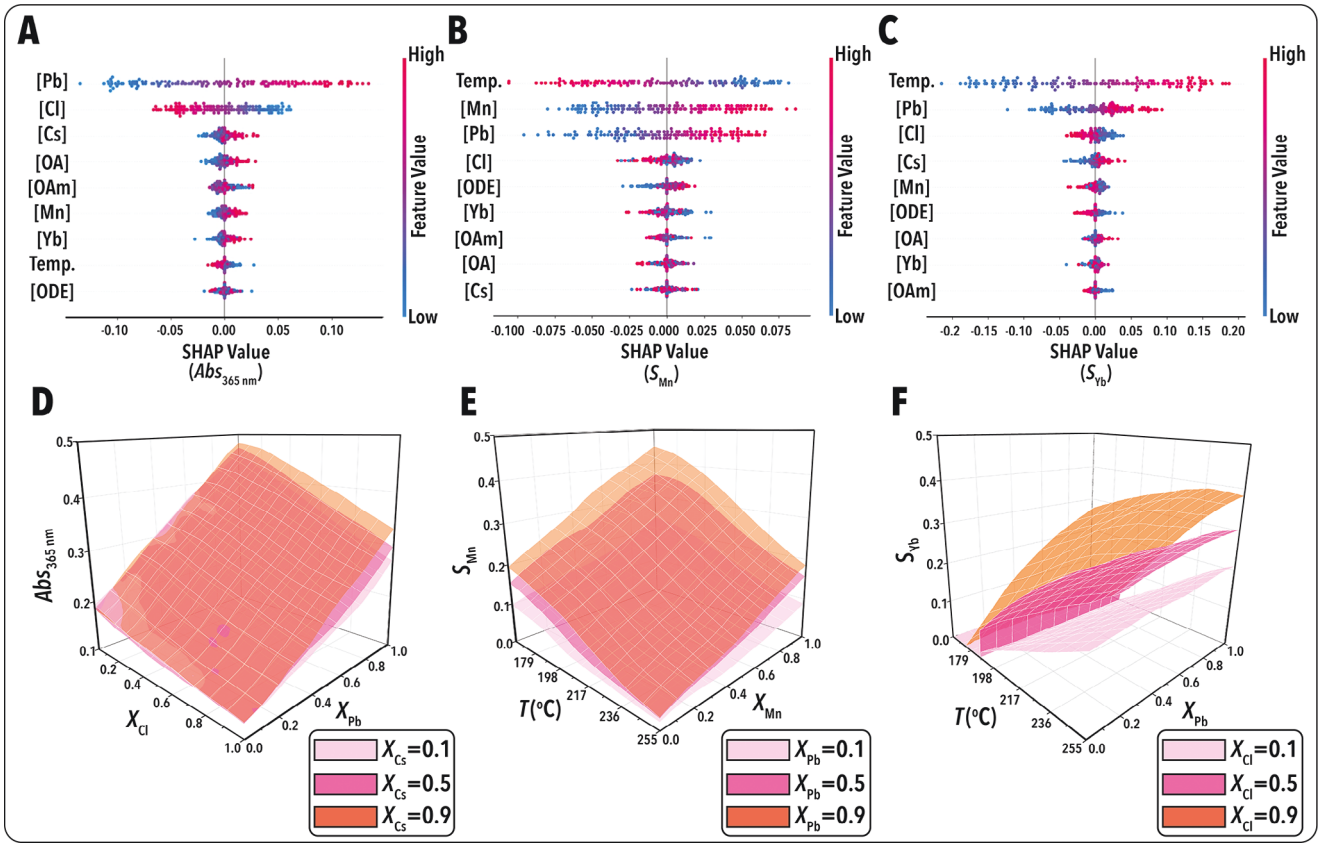

Figure 5. Accelerated mechanistic studies of high-temperature Mn-Yb co-doped $CsPbCl_3$ QD synthesis enabled by Smart Dope. Shapley additive explanation plots of QD optical parameters (outputs), including A) $Abs_{365\ nm}$, B) S_{Mn}, and C) S_{Yb}. Surface plots showing the impact of the most important synthesis input parameters on D) $Abs_{365\ nm}$, E) S_{Mn}, and F) S_{Yb}.

Five autonomous optimization campaigns, each with a budget of 10 iterations, were conducted using different decision-making policies: black-box random sampling, expected improvement (EI), upper confidence bound (UCB), pure exploitation (EPLT), and EI without prior knowledge (see Supplementary Information (Section S1.3, Supporting Information) for details of different experiment-selection decision policies). **Figure 6**A presents the Smart Dope's closed-loop performance for five different PLQY optimization campaigns of Mn-Yb co-doped $CsPbCl_3$ QDs. The EPLT experiment-selection policy reached a total PLQY of 130% in its eighth iteration. Subsequently, the UCB experiment-selection policy identified the synthetic route with the highest total PLQY of 153%, surpassing the maximum total PLQY obtained from the 150 LHS experiments. This result indicates that the global optima were not identified during the LHS stage, necessitating further exploration of the QD synthesis space. The EI experiment-selection policy reached the highest total PLQY of 158% after only four closed-loop iterations. However, the EI policy without prior knowledge (i.e., without the surrogate model trained on the LHS experimental data) and the black-box random sampling approach underperformed within the defined experimental budget, mainly due to the high-dimensionality nature of the experimental QD synthesis space. Figure 6B shows the UV-vis-NIR absorption and PL spectra of the highest-performing Mn-Yb co-doped $CsPbCl_3$ QDs autonomously synthesized by EI experiment-selection policy of Smart Dope. Table S6 (Supporting Information) summarizes the ML-identified QD synthesis conditions during each autonomous closed-loop optimization campaign of Smart Dope.

There are several reasons why the EI policy is considered a better option than the UCB policy for the autonomous optimization of multi-cation-doped LHP QDs. The EI policy directly measures the improvement of the defined objective function, which is crucial for optimizing the synthesis process. In contrast, the UCB policy primarily focuses on actions with higher uncertainty, which may not align perfectly with the objective-driven optimization. Lastly, the EI policy's emphasis on actions with the highest expected improvement over the current best value allows for faster convergence to the optimal conditions. With fewer experimental iterations, the EI policy can identify the optimal synthesis parameters more efficiently than the other tested experiment-selection strategies, thereby saving time and resources for the PLQY optimization of multi-cation-doped LHP QDs.[37] Additionally, by leveraging prior knowledge, incorporating the specific characteristics and constraints of the problem domain, and adapting based on past iterations, an informed EI decision-policy can significantly enhance decision-making during the autonomous optimization of Smart Dope compared to a black-box EI approach.[37] Based on the results summarized in Table S6 (Supporting Information), it can be inferred

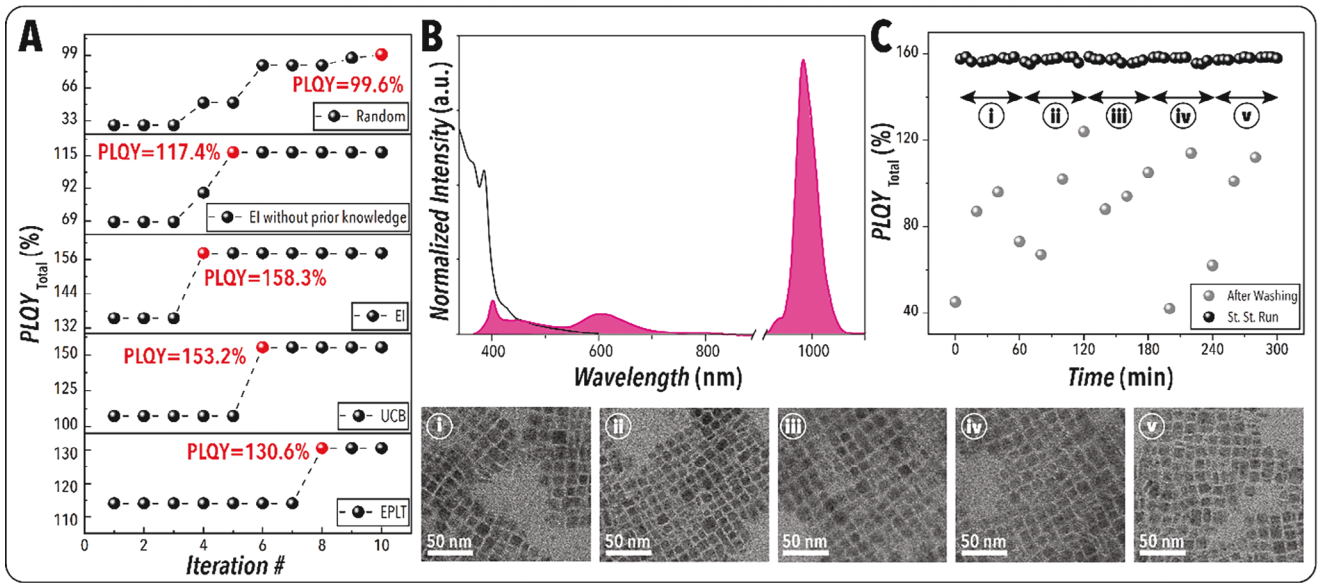

Figure 6. From autonomous optimization to continuous manufacturing. A) The representation of the best-condition-so-far for autonomous search of finding the highest total PLQY in each optimization campaign of Smart Dope under different experiment-selection policies. B) The in situ UV-vis-NIR absorption and PL spectra of the highest performing Mn-Yb co-doped LHP QDs discovered by informed EI experiment-selection policy of Smart Dope. C) Representation of stable and uniform Smart Dope's performance in terms of total PLQY for a 5-h continuous manufacturing process with automated intermittent washings. TEM images of the Mn-Yb co-doped LHP QDs captured after every hour of sample collection.

that the EI experiment-selection algorithm effectively limits the synthesis input parameters within a specific boundary, leading to the identification of global QD synthesis optima in the experimental synthesis space of Mn-Yb co-doped $CsPbCl_3$ QDs. It is important to note that due to the high dimensionality of the synthesis parameter space of Mn-Yb co-doped LHP QDs, relying solely on the prediction power of the digital twin does not immediately capture the global optima. Therefore, the closed-loop autonomous optimization approach offered by Smart Dope is necessary for the intelligent exploration of exponentially expanding parameter spaces while continuously updating and improving the prediction accuracy of the surrogate model.

One of the intriguing features of Smart Dope is its automated switching from autonomous optimization to continuous manufacturing operation modes. Once the most optimal synthetic route is identified via the autonomous optimization mode of Smart Dope, it can transition from exploration and optimization to continuous manufacturing mode. Figure 6C demonstrates the robust and precise performance of Smart Dope in continuous nanomanufacturing of the highest-performing Mn-Yb co-doped $CsPbCl_3$ QDs in-flow over 5 h time on stream with a throughput of 190 $mg.h^{-1}$, operating at a total liquid flowrate of 300 $\mu L\ min^{-1}$. The uniform cubic morphology of the in-flow synthesized QDs observed in the TEM images after every hour of sample collection supports Smart Dope's reliability and reproducibility in continuous nanomanufacturing. Smart Dope achieves the highest reported total PLQY value for Mn-Yb co-doped LHP QDs chemistry at an optimal temperature of 240 °C using the informed (trained surrogate model) EI experiment-selection policy of Smart Dope.

Drawing from the insights gained through the ML-driven belief model and the preliminary LHS experiments, as detailed in Table S4 (Supporting Information), it becomes evident that the contribution of Yb^{3+} ions to the total PLQY is negligible at temperatures below 190 °C. In this range, the dominant influence on the $PLQY_{total}$ appears to be primarily linked to the Mn emission. Conversely, a similar pattern of Yb emission selectivity emerges at temperatures exceeding 240 °C. Based on the autonomous QD mapping by Smart Dope, a higher contribution to the total PLQY of multi-cation-doped LHP QDs is observed with Yb doping (versus Mn doping). Furthermore, the incorporation of Yb^{3+} ions into the hose $CsPbCl_3$ QDs was found to reach its maximum level at elevated temperatures of 235 °C–240 °C (see Supporting Information, Table S4 and S5, Supporting Information). This discovery of the optimal QD synthesis condition highlights a reaction temperature region that colloidal nanoscience experts have not extensively investigated for metal cation doping of LHP QDs. This important result serves as an example of the power of autonomous experimentation (e.g., Smart Dope) in making unexpected discoveries via intelligent and material efficient navigation of high-dimensional parameter spaces.

Future work can focus on adopting the Smart Dope's platform to explore multi-cation doping of LHP QDs beyond 2 impurity lanthanide metal cation dopants as well as anion exchange with bromide ions to enhance the quality of the host LHP QDs and further improve the total PLQY of multi-cation-doped LHP QDs. We expect the future implications of Smart Dope to push further the performance of cation-doped LHP QDs serving as building blocks for the fabrication of high-performance energy harvesting devices such as downconverters and LSCs.

3. Conclusion

In summary, we successfully developed and deployed Smart Dope, which is an ML-assisted fluidic lab for autonomous parameter space exploration, development and optimization, mechanistic studies, and scalable manufacturing of multi-cation-doped

LHP QDs. Smart Dope's modular flow chemistry platform utilized a two-phase gas-liquid segmented flow format to enable precise control of the QD synthesis parameters at reaction temperatures up to 255 °C. By incorporating a pressure control module into the flow chemistry platform of Smart Dope, we accommodated the high-temperature QD synthesis and ensured the uniform and stable formation of reactive liquid slugs, required for continuous autonomous experimentation. The developed SDFL integrates a robust and reproducible process control, an in situ spectral data acquisition and processing unit, and an ML-assisted decision-making agent, enabling both automated and autonomous operation. Smart Dope leveraged an in situ spectral UV-vis-NIR characterization technique specifically tailored for lanthanide-doped LHP QDs, using miniature spectrometers, allowing continuous in situ absorption and PL spectroscopy of the in-flow synthesized QDs. Through our comprehensive studies involving ex situ structural characterizations and the knowledge obtained from the digital twin QD synthesis model, we proposed a homogeneous inward diffusion doping mechanism where Mn^{2+} and Yb^{3+} ions successfully undergo cation exchange with Pb^{2+} ions present in the host LHP QDs. Mn^{2+} ions form active complexes with available oleylammonium ions, while Yb^{3+} ions interact with Cl^- ions to facilitate the doping process. Leveraging Smart Dope's accelerated autonomous optimization mode, an informed EI experiment-selection strategy identified the optimal formulation of Mn-Yb co-doped $CsPbCl_3$ QDs with the highest reported PLQY of 158%. By intelligently navigating the experimental space of LHP QDs, Smart Dope successfully identified optimal synthetic conditions for multi-cation-doped LHP QDs, conducting 150 LHS experiments followed by 10 cycles of autonomous experimentation within an SDFL, over a 32-h timeframe without any human intervention. Subsequently, our platform seamlessly transitioned to continuous manufacturing mode, producing the optimal Mn-Yb co-doped LHP QDs at a throughput of 190 $mg.h^{-1}$ after purification. This study demonstrated the unique attributes and potential of Smart Dope in accelerating materials discovery and development related to renewable energy technologies by combining continuous robust experimentation and in situ characterization with modern data science tools to achieve closed-loop autonomous experimentation.

4. Experimental Section

Materials: All chemicals were used without further purification. 1-ocatedecene (ODE, 90%) and quinine sulfate (A0374529, absolute PLQY = 67.5%) were purchased from ACROS Organics. Oleic acid (OA, 90%) was purchased from Alfa Aesar. Oleylamine (OAm, 70%), cesium acetate (Cs(Ac), 99.99% trace metal basis, M_W = 191.95 g mol^{-1}), lead(II) acetate trihydrate ($Pb(Ac)_3.3H_2O$, 99.99% trace metal basis, M_W = 379.37 g mol^{-1}), ytterbium(III) acetate hydrate ($Yb(Ac)_3.XH_2O$, 99.95% trace metal basis, M_W = 350.17 g mol^{-1}), chlorotrimethylsilane (TMSCl, >98%), and manganese (II) acetate ($Mn(Ac)_2$, 98%, M_W = 173.027 g mol^{-1}) were purchased from Sigma-Aldrich. Hexane (ACS certified) and ethanol (70%) were purchased from Fisher Scientific. Sulfuric acid (H_2SO_4, 60%, 09 8361) was obtained from Oakwood Chemical. Toluene (HPLC grade) was purchased from VWR. Ar and nitrogen N_2 tanks were purchased from Airgas. SYLGARD 184 silicone elastomer and the curing agent were obtained from Ellsworth Adhesives. The organic dyes, HITC Perchlorate and IR-140 were purchased from EssilorLuxottica.

Precursor Preparation: The precursor preparation described herein was based on the study by Gamelin et al.,[19,20] with slight modifications made to adapt the QDs chemistry from batch to flow synthesis. Individual metal-containing precursors, Cs(Ac), $Pb(Ac)_2.3H_2O$, $Mn(Ac)_2$, and $Yb(Ac)_3.XH_2O$, were prepared by dissolving 0.28 mmol, 0.2 mmol, 0.02 mmol, and 0.1 mmol of the respective salts in ODE at 150 °C for 1 h. The dissolution process was carried out under a continuous flow of N_2 provided via a Schlenk line. The salts were dissolved in a ligand-solvent mixture of ODE:OA:OAm with a volumetric ratio of 24.5:1.0:0.5. For the chloride-based precursor, 500 µL of TMSCl was dissolved in 49 mL of ODE inside an N_2 glovebox. Two concentrated ligand-only precursors, ODE-OAm and ODE-OA, were prepared using a 5:1 ODE:ligand volumetric ratio. All the precursors, except for the pure ODE solution and the two ligand-only precursors, were loaded into gas-tight stainless steel syringes (50 mL, Chemyx) under inert conditions after reaching room temperature. All QD precursors were prepared in 60 mL glass septa vials.

Experimental Setup: The hardware of Smart Dope provides automatic access to 9 QD synthesis parameters and comprises four primary modules: 1) fluid delivery, 2) precursor formulation and reaction, 3) in situ characterization, and 4) pressure control. The fluid delivery module includes eight automated syringe pumps (Fusion 6000, Chemyx) equipped with stainless steel syringes (eight 50 mL, Chemyx) as well as one computer-controlled mass flow controller (MFC, Bronkhorst, EL-Flow Select). The fluid delivery module of Smart Dope was designed to precisely control the rate and stability of the QD precursor streams and the inert continuous phase (Ar) into the flow reactor. The minimum volumetric flow rate of the QD precursors regulated by the syringe pumps was set to 10 $\mu L.min^{-1}$ to ensure precise mixing of the QD precursors. The fluid delivery lines were connected to the formulation and reaction module using fluorinated ethylene propylene (FEP) tubing (0.02 in inner diameter, ID, 1/16 in outer diameter, OD, Microsolv Technology). The liquid precursor lines within the formulation and reaction module were initially connected to a 9-way fluidic manifold, creating an output stream of all QD precursors. The fluid stream leaving the manifold then passed through an in-line passive micromixer (FEP, 0.02 in ID) with a dead volume of 50 µL before transitioning into a gas-liquid segmented flow format inside the reaction module. To prevent the back-flow of liquid precursors into the gas line and ensure uniform flow segmentation during closed-loop autonomous experimentation, the Ar stream exiting the MFC was connected to an outlet check valve (IDEX). Considering the rapid formation kinetics of metal cation-doped LHP QDs, rapid mixing of QD precursors was crucial to ensure reproducible synthesis. Thus, it is decided to utilize a gas-liquid segmented flow format (instead of a single-phase flow) to achieve enhanced QD precursor mixing with the flow reactor. The gas-liquid segmented flow reactor was crucial in ensuring a reaction-limited regime for the uniform in-flow synthesis of multi-cation-doped LHP QDs evidenced by a narrow size distribution. The gas-liquid segmented flow was formed using a T-junction connected to the mixed QD precursors and Ar lines. The formed segmented flow was then passed to the reaction module (0.03″ ID × 1/16″ OD stainless steel tubing placed inside a helical-shaped aluminum reactor unit (see Figure S1, Supporting Information) for high-temperature synthesis of multi-cation-doped LHP QDs. Heating of the custom-machined reactor heating block was achieved using a cartridge heater (0.5″ diameter, 2″ long, 150 W, Omega) placed in the center of the reactor module (Figure S1, Supporting Information). The flow reactor module was thermally insulated, and the reaction temperature was automatically varied between 160 °C to 255 °C using a computer-controlled PID temperature controller (F4T, Watlow). The flow reactor (stainless steel tubing) inside the high-temperature reactor measured a total length of 0.5 m. The QD synthesis (residence) time was dynamically controlled without sacrificing the segmented flow uniformity by varying the total liquid volumetric flow rates (ranging from 150 $\mu L.min^{-1}$ to 400 $\mu L.min^{-1}$) while maintaining a constant gas-to-liquid volumetric ratio of 1.2. The flow reactor outlet was connected to perfluoroalkoxy (PFA) tubing (0.03″ ID × 1/16″ OD, Microsolv Technology) via a stainless steel union. The produced QDs within the reactive liquid slugs leaving the flow reactor module of Smart Dope were rapidly cooled down to room temperature before entering the in situ characterization module (flowcell, 0.04″ ID × 1/16″ OD, FEP tubing, Microsolv Technology). The total volume of the flow chemistry setup after the flow segmentation section until the in situ characterization module was

nearly 620 µL. The custom-built flowcell was connected via three fibers to: 1) a high-power UV light emitting diode (UV LED, 365 nm, Thorlabs, M365LP1, 90° configuration) serving as the PL excitation light source, 2) a balanced UV-vis light source (Ocean Insight, DH-2000BAL, 180° configuration), and 3) a miniature spectrometer (Ocean Insight, Ocean HDX Miniature Spectrometer, 180° configuration) for real-time spectral monitoring of the UV-vis-NIR absorption and PL spectra of the in-flow synthesized multi-cation-doped LHP QDs. Integration times of 6 ms and 20 ms were used for UV-vis and PL spectra acquisition, respectively. The three optical features that were automatically calculated from the in situ obtained UV-vis-NIR absorption and PL spectra are: i) $Abs_{365\ nm}$, ii) S_{Mn}, iii) S_{Yb}. Smart Dope's hardware was pressurized using a back pressure regulator (Equilibar) at 95 psig N_2. The incorporation of the back-pressure module mitigates volumetric changes in the gas phase at high reaction temperatures, thereby ensuring uniform liquid slug size and residence time during the high-temperature QD synthesis in the flow reactor.

Supporting Information

Supporting Information is available from the Wiley Online Library or from the author.

Acknowledgements

F.B. and S.S. contributed equally to this work. The authors gratefully acknowledge the financial support provided by the National Science Foundation (award # 1940959), the UNC Research Opportunities Initiative (UNC-ROI) grant, and the Dreyfus Program for Machine Learning in the Chemical Sciences and Engineering (Award # ML-21-064). This work was performed in part at the Analytical Instrumentation Facility (AIF) at North Carolina State University, which is supported by the State of North Carolina and the National Science Foundation (award number ECCS-1542015). The AIF is a member of the North Carolina Research Triangle Nanotechnology Network (RTNN), a site in the National Nanotechnology Coordinated Infrastructure (NNCI). EPR spectroscopy was performed in part by the Molecular Education, Technology and Research Innovation Center (METRIC) at NC State University, which is supported by the State of North Carolina.

Conflict of Interest

The authors declare no conflict of interest.

Data Availability Statement

The data that support the findings of this study are available in the supplementary material of this article.

Keywords

autonomous experimentation, modular flow chemistry, multi-cation-doped perovskite quantum dots, self-driving labs

Received: July 18, 2023
Revised: October 5, 2023
Published online: November 12, 2023

[1] M. V. Kovalenko, L. Protesescu, M. I. Bodnarchuk, *Science* **2017**, *358*, 745.
[2] A. F. Gualdrón-Reyes, S. Masi, I. Mora-Seró, *Trends Chem* **2021**, *3*, 499.
[3] L. De Trizio, I. Infante, A. L. Abdelhady, S. Brovelli, L. Manna, *Trends Chem* **2021**, *3*, 631.
[4] Y. Zhang, T. D. Siegler, C. J. Thomas, M. K. Abney, T. Shah, A. De Gorostiza, R. M. Greene, B. A. Korgel, *Chem. Mater.* **2020**, *32*, 5410.
[5] K. Abdel-Latif, F. Bateni, S. Crouse, M. Abolhasani, *Matter* **2020**, *3*, 1053.
[6] Y. Bai, M. Hao, S. Ding, P. Chen, L. Wang, *Adv. Mater.* **2021**, 2105958.
[7] A. Pan, B. He, X. Fan, Z. Liu, J. J. Urban, A. P. Alivisatos, L. He, Y. Liu, *ACS Nano* **2016**, *10*, 7943.
[8] H. Huang, R. Li, S. Jin, Z. Li, P. Huang, J. Hong, S. Du, W. Zheng, X. Chen, D. Chen, *ACS Appl. Mater. Interfaces* **2021**, *13*, 34561.
[9] S. Yakunin, L. Protesescu, F. Krieg, M. I. Bodnarchuk, G. Nedelcu, M. Humer, G. De Luca, M. Fiebig, W. Heiss, M. V. Kovalenko, *Nat. Commun.* **2015**, *6*, 8056.
[10] P. Ramasamy, D.-H. Lim, B. Kim, S.-H. Lee, M.-S. Lee, J.-S. Lee, *Chem. Commun.* **2016**, *52*, 2067.
[11] T. Cai, J. Wang, W. Li, K. Hills-Kimball, H. Yang, Y. Nagaoka, Y. Yuan, R. Zia, O. Chen, *Adv. Sci.* **2020**, *7*, 2001317.
[12] T. Wei, K. Lian, J. Tao, H. Zhang, D. Xu, J. Han, C. Fan, Z. Zhang, W. Bi, C. Sun, *ACS Appl. Mater. Interfaces* **2022**, *14*, 44572.
[13] V. I. Klimov, T. A. Baker, J. Lim, K. A. Velizhanin, H. Mcdaniel, *ACS Photonics* **2016**, *3*, 1138.
[14] F. Bateni, R. W. Epps, K. Abdel-latif, R. Dargis, S. Han, A. A. Volk, M. Ramezani, T. Cai, O. Chen, M. Abolhasani, *Matter* **2021**, *4*, 2429.
[15] S. Das Adhikari, A. K. Guria, N. Pradhan, *J. Phys. Chem. Lett.* **2019**, *10*, 2250.
[16] D. Parobek, B. J. Roman, Y. Dong, H. Jin, E. Lee, M. Sheldon, D. H. Son, *Nano Lett.* **2016**, *16*, 7376.
[17] D. Zhou, D. Liu, G. Pan, X. Chen, D. Li, W. Xu, X. Bai, H. Song, *Adv. Mater.* **2017**, *29*, 1704149.
[18] G. Pan, X. Bai, D. Yang, X. Chen, P. Jing, S. Qu, L. Zhang, D. Zhou, J. Zhu, W. Xu, B. Dong, H. Song, *Nano Lett.* **2017**, *17*, 8005.
[19] T. J. Milstein, D. M. Kroupa, D. R. Gamelin, *Nano Lett.* **2018**, *18*, 3792.
[20] T. J. Milstein, K. T. Kluherz, D. M. Kroupa, C. S. Erickson, J. J. De Yoreo, D. R. Gamelin, *Nano Lett.* **2019**, *19*, 1931.
[21] D. Zhou, R. Sun, W. Xu, N. Ding, D. Li, X. Chen, G. Pan, X. Bai, H. Song, *Nano Lett.* **2019**, *19*, 6904.
[22] W. J. Mir, T. Sheikh, H. Arfin, Z. Xia, A. Nag, *NPG Asia Mater* **2020**, *12*, 9.
[23] X. Zhuang, R. Sun, D. Zhou, S. Liu, Y. Wu, Z. Shi, Y. Zhang, B. Liu, C. Chen, D. Liu, H. Song, *Adv. Funct. Mater.* **2022**, *32*, 2110346.
[24] T. J. Milstein, J. Y. D. Roh, L. M. Jacoby, M. J. Crane, D. E. Sommer, S. T. Dunham, D. R. Gamelin, *Chem. Mater.* **2022**, *34*, 3759.
[25] F. Bateni, R. W. Epps, K. Antami, R. Dargis, J. A. Bennett, K. G. Reyes, M. Abolhasani, *Adv. Intell. Syst.* **2022**, *4*, 2200017.
[26] A. A. Volk, R. W. Epps, M. Abolhasani, *Adv. Mater.* **2021**, *33*, 2004495.
[27] F. Delgado-Licona, M. Abolhasani, *Adv. Intell. Syst.* **2023**, *5*, 2200331.
[28] K. Antami, F. Bateni, M. Ramezani, C. E. Hauke, F. N. Castellano, M. Abolhasani, *Adv. Funct. Mater.* **2022**, *32*, 2108687.
[29] J. A. Bennett, M. Abolhasani, *Curr. Opin. Chem. Eng.* **2022**, *36*, 100831.
[30] R. W. Epps, M. Abolhasani, *Appl. Phys. Rev.* **2021**, *8*, 041316.
[31] A. A. Volk, Z. S. Campbell, M. Y. S. Ibrahim, J. A. Bennett, M. Abolhasani, *Annu. Rev. Chem. Biomol. Eng.* **2022**, *13*, 45.
[32] R. W. Epps, M. S. Bowen, A. A. Volk, K. Abdel-Latif, S. Han, K. G. Reyes, A. Amassian, M. Abolhasani, *Adv. Mater.* **2020**, *32*, 2001626.
[33] R. W. Epps, A. A. Volk, M. Y. S. Ibrahim, M. Abolhasani, *Chem.* **2021**, *7*.
[34] A. A. Volk, R. W. Epps, D. T. Yonemoto, B. S. Masters, F. N. Castellano, K. G. Reyes, M. Abolhasani, *Nat. Commun.* **2023**, *14*, 1403.
[35] M. Abolhasani, K. A. Brown, *MRS Bull.* **2023**, *48*, 134.

[36] M. Abolhasani, E. Kumacheva, *Nat. Synth.* **2023**, *2*, 483.
[37] R. W. Epps, A. A. Volk, K. G. Reyes, M. Abolhasani, *Chem. Sci.* **2021**, *12*, 6025.
[38] K. Abdel-Latif, R. W. Epps, F. Bateni, S. Han, K. G. Reyes, M. Abolhasani, *Adv. Intell. Syst.* **2021**, *3*, 2000245.
[39] M. Krenn, R. Pollice, S. Y. Guo, M. Aldeghi, A. Cervera-Lierta, P. Friederich, G. Dos Passos Gomes, F. Häse, A. Jinich, A. Nigam, Z. Yao, A. Aspuru-Guzik, *Nat. Rev. Phys.* **2022**, *4*, 761.
[40] H. Lv, X. Chen, *Nanoscale* **2022**, *14*, 6688.
[41] Z. Tu, T. Stuyver, C. W. Coley, *Chem. Sci.* **2023**, *14*, 226.
[42] Z. Yao, Y. Lum, A. Johnston, L. M. Mejia-Mendoza, X. Zhou, Y. Wen, A. Aspuru-Guzik, E. H. Sargent, Z. W. Seh, *Nat. Rev. Mater.* **2022**, *8*, 202.
[43] H. Tao, T. Wu, S. Kheiri, M. Aldeghi, A. Aspuru-Guzik, E. Kumacheva, *Adv. Funct. Mater.* **2021**, *31*, 2106725.
[44] A. E. Gongora, B. Xu, W. Perry, C. Okoye, P. Riley, K. G. Reyes, E. F. Morgan, K. A. Brown, *Sci. Adv.* **2020**, *6*, eaaz1708.
[45] D. Salley, G. Keenan, J. Grizou, A. Sharma, S. Martín, L. Cronin, *Nat. Commun.* **2020**, *11*, 2771.
[46] B. P. Macleod, F. G. L. Parlane, C. C. Rupnow, K. E. Dettelbach, M. S. Elliott, T. D. Morrissey, T. H. Haley, O. Proskurin, M. B. Rooney, N. Taherimakhsousi, D. J. Dvorak, H. N. Chiu, C. E. B. Waizenegger, K. Ocean, M. Mokhtari, C. P. Berlinguette, *Nat. Commun.* **2022**, *13*, 995.
[47] Y. Jiang, D. Salley, A. Sharma, G. Keenan, M. Mullin, L. Cronin, *Sci. Adv.* **2022**, *8*, eabo2626.
[48] K. Abdel-Latif, R. W. Epps, C. B. Kerr, C. M. Papa, F. N. Castellano, M. Abolhasani, *Adv. Funct. Mater.* **2019**, *29*, 1900712.
[49] Z. S. Campbell, F. Bateni, A. A. Volk, K. Abdel-Latif, M. Abolhasani, *Part. Part. Syst. Charact.* **2020**, *37*, 2000256.
[50] K. Hills-Kimball, M. J. Pérez, Y. Nagaoka, T. Cai, H. Yang, A. H. Davis, W. Zheng, O. Chen, *Chem. Mater.* **2020**, *32*, 2489.
[51] J. De Roo, M. Ibáñez, P. Geiregat, G. Nedelcu, W. Walravens, J. Maes, J. C. Martins, I. Van Driessche, M. V. Kovalenko, Z. Hens, *ACS Nano* **2016**, *10*, 2071.
[52] W. Van Der Stam, J. J. Geuchies, T. Altantzis, K. H. W. Van Den Bos, J. D. Meeldijk, S. Van Aert, S. Bals, D. Vanmaekelbergh, C. De Mello Donega, *J. Am. Chem. Soc.* **2017**, *139*, 4087.